First-principles study of mechanical and electronic properties of bent monolayer transition metal dichalcogenides

Niraj K. Nepal,[1,*] Liping Yu,[2] Qimin Yan,[1] and Adrienn Ruzsinszky[1]
[1]*Department of Physics, Temple University, Philadelphia, Pennsylvania 19122, USA*
[2]*Department of Physics and Astronomy, University of Maine, Orono, Maine 04469, USA*

The mechanical and electronic properties of transition metal dichalcogenide (TMD) monolayers corresponding to transition groups IV, VI, and X are explored under mechanical bending from first principles calculations using the strongly constrained and appropriately normed (SCAN) meta-GGA. SCAN provides an accurate description of the phase stability of the TMD monolayers. Our calculated lattice parameters and other structural parameters agree well with experiment. We find that bending stiffness (or flexural rigidity) increases as the transition metal group goes from IV to X to VI, with the exception of $PdTe_2$. Variation in mechanical properties (local strain, physical thickness) and electronic properties (local charge density, band structure) with bending curvature is discussed. The local strain profile of these TMD monolayers under mechanical bending is highly nonuniform. The mechanical bending tunes not only the thickness of the TMD monolayers, but also the local charge distribution as well as the band structures, adding more functionalization options to these materials.

I. INTRODUCTION

Layered transition metal dichalcogenides (TMD) offer a wide variety of physical and chemical properties from metal to insulator [1–3] and are extensively studied [4–7]. An increasing interest and recent progress toward these materials led to a variety of improved applications such as sensors, energy storage, photonics, optoelectronics, and spintronics [8–10]. In particular, atomically thin monolayer TMDs have attracted most of the attention due to the unique mechanical and electronic properties related to their high flexibility [11–13]. A large scope of flexible electronics has been realized via applications such as flexible displays [14–17], wearable sensors [18–20], and electronic skins [21–23]. Each TMD (TX_2) monolayer consisting of three atomic layers (X-T-X stacking) can undergo bending deformation, possessing higher flexural rigidity than graphene ($D_{MoS_2} \sim 7$–8 $D_{graphene}$ [24]). The bending behavior (curvature effect) of 2D TMD monolayers, especially of MoS_2, has been studied both theoretically [25,26] and experimentally [12,27]. For 2D materials such as MoS_2, the bending can induce localization or delocalization in the electronic charge distribution. This change in the charge distribution results in changes in electronic properties such as the Fermi level, effective mass, and band gap [28]. However, the bending behavior of other TMD monolayers is largely unexplored at least from first principles. Quantitatively, the resistance of a material against bending is characterized by the bending stiffness. The bending stiffness or flexural rigidity of the TMD monolayers can be estimated using first-principles calculation as in Refs. [25,29,30]. Most of the earlier studies used nanotubes of different radii created by rolling an infinitely extended sheet to estimate the bending stiffness of

2D monolayers [29–31]. However, such a scheme has several limitations. (1) It does not mimic the edges present in the monolayer. (2) The nanoribbons unfolded from differently sized nanotubes have different widths which contribute to different quantum confinement effects along with the curvature effect. By utilizing the bending scheme similar to the bending of a thin plate, we restore the edges as well as fix the width of the nanoribbon, thereby eliminating the quantum confinement effect resulting from difference in width between various configurations of nanoribbons from flat to bent ones. However, the edge effects due to their finite width may not be completely eliminated.

Here we report a comprehensive first-principles study of the structural, mechanical, and electronic properties of flat and bent monolayer TMD compounds, i.e., TX_2 (T = transition metal, X = chalcogen atom). As in Ref. [1], we represent each TMD (TX_2) with its transition metal group. For example, d^0 for group IV, d^2 for group VI, and d^6 for group X. Their layer structures have been observed in experiment: group IV (T = Ti, Zr or Hf; X = S, Se or Te) and group X ($PdTe_2$ and PtX_2) TMDs prefer the 1T phase, while group VI TMDs crystallize in the 1H (T = Mo or W; X = S, Se) as well as the distorted T (1T′) phase (WTe_2) [1]. We first investigate the relative stability of a monolayer in three different phases (1H, 1T, 1T′). The mechanical and electronic properties have been studied only for those most stable phases. The organization of the rest of the paper is as follows. The computational details are presented in Sec. II. Section III presents our results, followed by some discussion and conclusions in Sec. IV.

II. COMPUTATIONAL DETAILS

The ground-state calculations were performed using the Vienna *ab initio* simulation package (VASP) [32] with

---
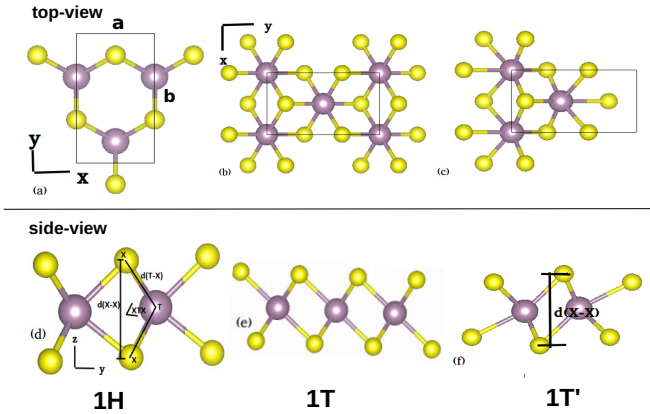
*Corresponding author: niraj.nepal@temple.edu

FIG. 1. Rectangular unit-cells of types 1H, 1T, and 1T′ (WTe$_2$) used in the calculations. The first row represents the top view (a)–(c) while second (d)–(f) corresponds to the side view; d(T-X) is metal-chalcogen distance, ∠XTX is an angle made by two d(T-X) sides, and d(X-X) (or d$_{X-X}$) is the distance between the outer and inner layer of flat monolayer bulk TMDs.

projector augmented wave (PAW) [33] pseudopotentials (PS) [34] as implemented in the VASP code [35], modified to include the kinetic energy density required for meta-GGA (MGGA) calculations. We used pseudopotentials recommended in VASP for all elements except for tungsten (W), where we used a pseudopotential such that the valence electron configuration includes $6s^1 5d^5$ electrons. The exchange-correlation energy was approximated using the strongly constrained and appropriately normed (SCAN) MGGA [36]. It can describe an intermediate range of dispersion via the kinetic energy density and is proven to deliver sufficiently accurate ground-state properties for diversely bonded systems [37–40], as compared to local density approximation (LDA) and the generalized gradient approximation (GGA) of Perdew, Burke, and Ernzerhof (PBE). The unit-cell calculations for all pristine TMD monolayers were carried out using a rectangular supercell consisting of two MX$_2$-units with three different configurations 1H, 1T, and 1T′-WTe$_2$ to determine the most stable ground state. We used the energy cutoff of 550 eV and $24 \times 16 \times 1$ and $16 \times 24 \times 1$ Γ-centered Monkhorst-Pack k-meshes [41] to sample the Brillouin zone. Periodic boundary conditions were applied along the in-plane direction, while a vacuum of about 20 Å was inserted along the out-of-plane direction. The geometry optimization of the mono-layer unit-cell was achieved by converging all the forces and energies within 0.005 eV/Å and 10^{-6} eV, respectively. To estimate the bending stiffness, we relaxed our nanoribbons having a width of 3–4 nm (Supplemental Material Table S1 [62]) with forces less than 0.01 eV/Å, using an energy cutoff of 450 eV. The Brillouin zone was sampled using Γ-centered Monkhorst-Pack k-meshes of $8 \times 1 \times 1$ and $1 \times 8 \times 1$.

To estimate the in-plane stiffness, we applied strain along one direction (say the x direction) and relaxed the system along the lateral direction (i.e., the y direction) or vice versa (see Fig. 1). An in-plane stiffness then can be estimated using

$$Y_{2D} = \frac{1}{A_0} \frac{\partial^2 E_s}{\partial \epsilon^2}, \tag{1}$$

where $E_s = E(\epsilon = s) - E(\epsilon = 0)$ is the strain energy, $\epsilon = \frac{\text{change in length}(\Delta l)}{\text{equilibrium length}(l_0)}$ is the linear strain, and A_0 is an equilibrium area of an unstrained supercell. We also applied a 5% axial strain and relaxed the rectangular supercell in the transverse direction to estimate the lateral strain and hence found the Poisson's ratio. We first relaxed the flat ribbon using various edge schemes. The choices of edges are mainly due to either relaxation of the flat nanoribbon or to satisfy the condition, areal bending energy density $u(\kappa) = \frac{E_{\text{bent}} - E_{\text{flat}}}{\text{area}(A)} \to 0$ as the bending curvature $\kappa = \frac{1}{\text{radius of curvature }(R)} \to 0$ [Fig. 2(IV)]. We have taken stoichiometric ($n(\text{X}):n(T) = 2:1$) nanoribbons (Supplemental Material Fig. S4 [62]) for most of the calculations in which TiTe$_2$, MoTe$_2$-1T′, and WX$_2$ (X = S, Se, or Te) were stabilized using hydrogen passivated edges, whereas others were relaxed without hydrogen passivation. We also relaxed TiSe$_2$, HfS$_2$, PdTe$_2$, and PtSe$_2$ nanoribbons in symmetric configuration [Fig. 2(II)]. Finally, the bent structures of different bending curvatures were created by relaxing the ribbons along the infinite length direction, while keeping the transition atoms fixed at the opposite end, and applying strain along the width direction. A 20 Å of vacuum was introduced along the y and z direction to eliminate an interaction between the system and its image (Supplemental Material Fig. S4 [62]). The areal bending energy density [$u(\kappa)$] versus bending curvature (κ) curve were fitted with a cubic polynomial to capture the nonlinear behavior [Fig. 2(IV)]. The quadratic coefficient of the cubic fitting was utilized to estimate the bending stiffness,

$$S_b = \frac{\partial^2 u(\kappa)}{\partial \kappa^2}\bigg|_{\kappa=0}. \tag{2}$$

III. RESULTS

A. Relative stability

Experimentally, it is largely known which phase is preferred in the bulk layer structure. However, the relative stability of their monolayer structures remained elusive. We have performed relative stability analysis of monolayer TX$_2$ among three different phases, namely, 1H, 1T, and 1T′-WTe$_2$, to test the predictive power of SCAN. Energies of TMDs in different phases relative to the 1T phase are presented in Fig. 3. Among two different phases, 1H and 1T, group (IV) and (X) TMD monolayers prefer the 1T phase. We could not find a distorted phase (1T′) for these TMD monolayers. In addition to the 1H and 1T phase, group (VI) TMDs MoTe$_2$ and WTe$_2$ also crystallize in the distorted (1T′) form. Our relative stability analysis shows that TX$_2$ with X = S or Se prefers the 1H phase, while it depends on the transition metal for X = Te, consistent with the experimental predictions [1]. WTe$_2$ prefers the 1T′ phase while the cohesive energies of 1H and 1T′ phases of MoTe$_2$ are almost identical (favoring the 1H phase by 5 meV), leading to an easy modulation between 2 phases [42]. Satisfying 17 exact known constraints, SCAN accurately captures the necessary interactions present in these TMD monolayers and predicts the correct ground-state structure.
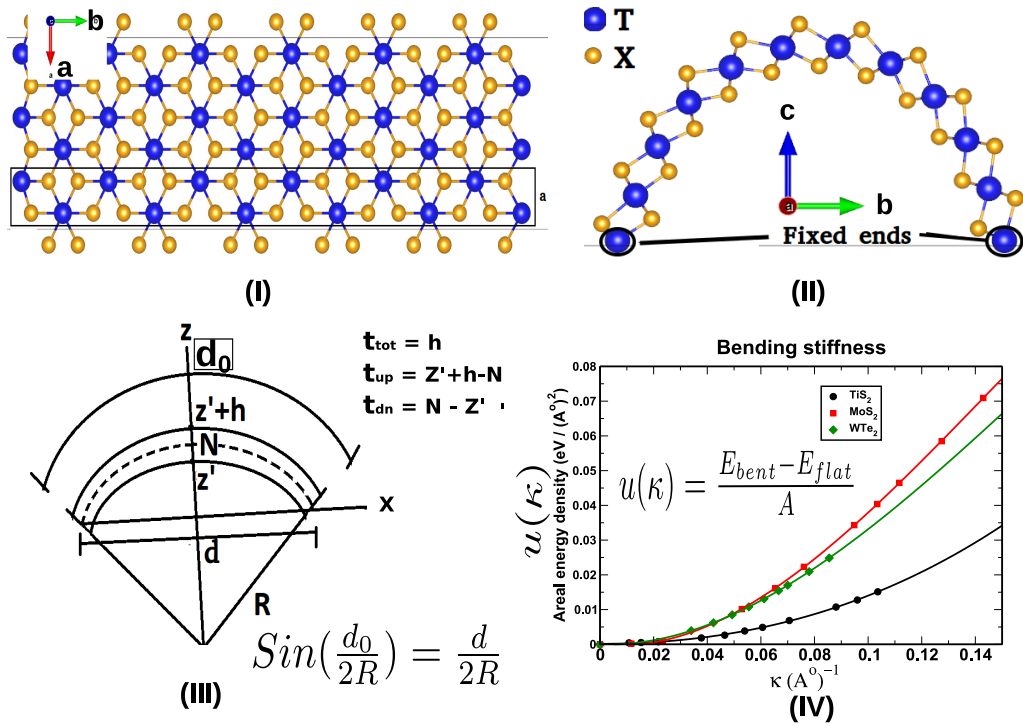
FIG. 2. (I) A nanoribbon (enclosed by rectangle) is taken to simulate an extended sheet of 1T monolayer; a is the lattice constant with the ribbon extended along the *a* axis and a vacuum of 20 Å is inserted along *b* and *c* axes (Supplemental Material Fig. S4 [62]); bent sample of 1T nanoribbon; (III) a schematic bending of a thin plate. d0, d, and R are the length of a thin plate before bending, length after bending, and radius of curvature, respectively. *N* is the neutral surface denoted by a dashed line. t_{tot}, t_{up}, and t_{dn} are the physical thicknesses of the bent nanoribbon, assuming that the middle layer coincides with the neutral surface (*N*); (IV) areal bending energy density vs bending curvature curve to estimate the bending stiffness. E_{bent}, E_{flat}, and *A* are the total energy of bent nanoribbon, total energy of flat nanoribbon, and cross-sectional area of flat nanoribbon (length × width), respectively.

B. Structural properties

Comparison has been made for the estimated in-plane lattice constant of monolayers with the experimental bulk results in Fig. 4. The lattice constants are in good agreement with the experimental results with a mean absolute error (MAE) and a mean absolute percentage error (MAPE) of 0.03 Å and 0.7%, respectively. The results for the structural parameters related to the monolayer bulk are in good agreement with reference values [8]. The structural parameters related to the lattice constant such as d_{T-X}, d_{X-X}, and θ_{X-T-X} increase from S to Se to Te. The decreasing cohesive energies from S to Se to Te make them more loosely bound, thereby increasing the lattice parameters.

C. In-plane stiffness and Poisson's ratio

The strength of a material is crucial for a device's performance and its durability. As a measure of the strength, we computed an in-plane stiffness or 2D Young's modulus [Eq. (1)] of the most stable ground state and tabulated it in Table I. Similar to the cohesive energy, the in-plane stiffness decreases from S to Se to Te, indicating a softening of TMD monolayers from S to Te under an application of linear strain. The estimated 2D in-plane stiffness of MoS$_2$ is 141.59 N/m, which is in close agreement with the experimental value of 180 ± 60 N/m [45].

Under Poisson's effect, materials tend to expand (or contract) in a direction perpendicular to the axis of compression

(or expansion). It can be measured using Poisson's ratio $\nu_{ij} = -\frac{d\epsilon_j}{d\epsilon_i}$, where $d\epsilon_j$ and $d\epsilon_i$ are transverse and axial strains, respectively. The in-plane ($-\frac{d\epsilon_y}{d\epsilon_x}$ or $-\frac{d\epsilon_x}{d\epsilon_y}$) and an out of plane Poisson's ratio ($-\frac{d\epsilon_z}{d\epsilon_x}$) are also calculated and tabulated. The in-plane Poisson's ratio is different than that of the out-of-plane Poisson's ratio for 1T compounds. For example, PtS$_2$ has $\nu_{xy} = 0.29$ and $\nu_{xz} = 0.58$. However, the Poisson's ratio of 1H monolayers is almost isotropic ($\nu_{xy} \approx \nu_{xz}$).

D. Mechanical bending

The primary focus of this study is to understand the response of the TMD monolayers to mechanical bending. We have calculated the bending stiffness and studied the change in various physical and electronic properties due to bending. Since previous studies [27,28] showed that the bending stiffness is independent of the type of the armchair or zigzag edges (chiral), we only utilized armchair-edge nanoribbons for the 1H structures. The bending stiffness of 20 TMDs are compared and tabulated in Table I. Unlike the in-plane stiffness, the overall bending stiffness increases from S to Se to Te (Table I), indicating a hardening of the nanoribbons from S to Se to Te. The d^0 compounds, especially S and Se, along with the PdTe$_2$ have lower (<3 eV) bending stiffness. The lower flexural rigidity of these compounds can result in enormous changes in their local strain as well as the charge density profile under mechanical bending. The 1H compounds have
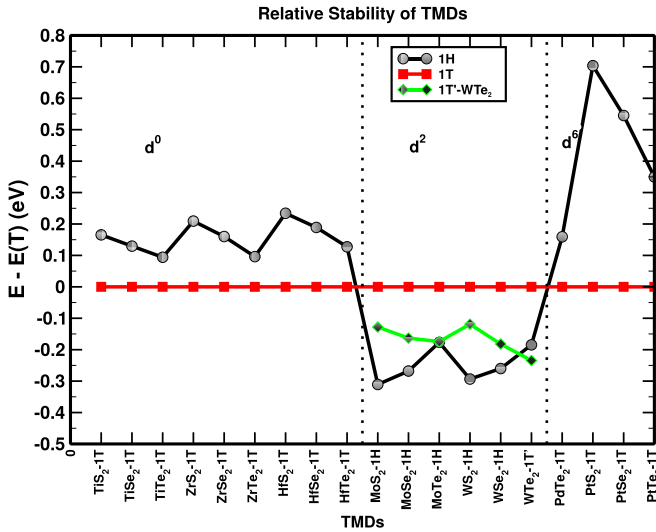
FIG. 3. Stability (relative to the 1T phase) from SCAN calculations for TMDs between the 3 experimentally observed phases 1H, 1T, and 1T'-WTe$_2$. The x axis represents the TMD with a phase corresponding to the minimum ground-state (GS) energy, and the relative GS energies per atom of the TMDs of any phase with respect to corresponding GS of 1T phase are presented on the y axis. The straight line parallel to the x-axis passing through the origin represents the GS energies of 1T phases. SCAN correctly predicts the ground state for these compounds. Also, MoTe$_2$ seems to be isoenergetic between 1H and 1T'-WTe$_2$ phases.

higher bending stiffness, possessing higher flexural rigidity against mechanical bending. The estimated bending stiffness of 12.29 eV for MoS$_2$ agrees with the experimental values of 6.62–13.24 eV [12] as well as 10–16 eV [27]. To explore the trend of mechanical strengths with respect to transition metal, one can look into the d-band filling of valence electrons. The filling of the d band increases from transition metal group IV (~sparsely-filled) to VI (~half-filled) to X (~completely filled) within the same row in periodic table. Both quantities
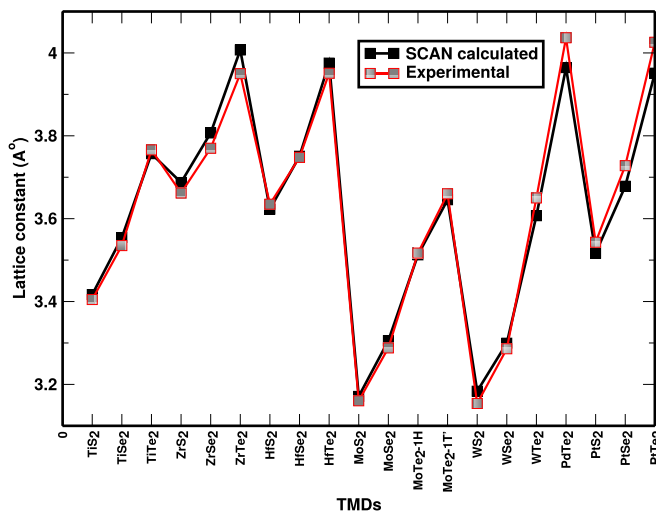

FIG. 4. Comparison of the SCAN-calculated in-plane lattice constants of various TMD monolayers in the ground state with respect to the bulk lattice constants available in the literature [1,43,44].

Y$_{2D}$ and S$_b$ increase as the number of valence d electrons increases until the shell becomes nearly half-filled. To facilitate the claim further, we have estimated the in-plane stiffness and bending stiffness of 1H-NbS$_2$ and 1H-TaS$_2$ corresponding to group V (d^1) transition metals. The in-plane stiffness of NbS$_2$ and TaS$_2$ were found to be 95.74 N/m and 115.04 N/m, respectively. In addition, the bending stiffness was obtained as 4.87 eV and 6.43 eV, respectively, for NbS$_2$ and TaS$_2$. Comparing TMDs (TX$_2$) having the same chalcogen atom, we can see the trend d^0 < d^1 < d^2 for both stiffness. However, there is a decrement in both Y$_{2D}$ and S$_b$ while going from half-filled (d^2) to nearly completely filled (d^6) d-band transition metal. Moreover, the large bending stiffness of group VI compounds decreases on changing phase from 1H to distorted 1T phase, for instance, 1H to 1T' transformation in MoTe$_2$.

We utilized

$$t_{\text{eff}} = \sqrt{12 S_b / Y_{2D}} \tag{3}$$

and

$$Y_{3D} = Y_{2D} / t_{\text{eff}} \tag{4}$$

to estimate the effective thickness as well as the 3D Young's modulus. An effective thickness is the combination of d$_{X\text{-}X}$ distance and the total effective decay length of electron density into the vacuum. Experimentally, it is difficult to define the total effective decay length of the electronic charge distribution. Therefore, it is a common practice to take a range from the d$_{X\text{-}X}$ distance to the inter layer metal-metal distance within the bulk structure as the effective thickness, which gives the range for both in-plane stiffness and bending stiffness [12,27]. Using Eq. (3), one can estimate a reasonable value for the effective thickness for a wide range of TMDs. However, the computed effective thicknesses t_{eff} of certain TX$_2$ (T=Ti, Zr, Hf; X=S, Se) are less than their d$_{X\text{-}X}$ distance (Fig. 1), which means that bending is much easier than stretching. Similar underestimation was found for the effective thickness of a carbon monolayer estimated by various methods [46–49]. Utilizing Eq. (3), Yakobson et $al.$ [46], Wang [47], and Yu et $al.$ [28] estimated the effective thickness of the carbon monolayer to be around 0.7–0.9 Å, which is much less than 3.4 Å, the normal spacing between sheets in graphite. Such huge underestimation indicates the possible breakdown of Eq. (3) to estimate the effective thickness in the case of atomically thin carbon layer [47]. The 3D Young's modulus [Eq. (4)] allows us to compare the strength between various 2D and 3D materials, for instance, MoS$_2$ against steel. Similar to 2D in-plane stiffness, the 3D Young's modulus of TMD monolayers decreases from S to Se to Te. Due to the larger underestimation of the effective thickness, there is a huge overestimation in the 3D Young's modulus of group IV compounds with sulfur as the chalcogen atom. With that in mind, one can conclude that MoS$_2$ as well as WS$_2$ have large 3D Young's moduli of 347.03 and 351.02 GPa, respectively, agreeing with the experimental value of 270 ± 100 GPa [45] for MoS$_2$.

TABLE I. The ground-state properties of TMD mono-layers having 1H or 1T phase: Relaxed in-plane lattice constant, a; Metal-chalcogen and chalcogen-chalcogen distance, d_{T-X} and d_{X-X}, respectively (see Fig. 1); X-T-X angle, θ_{X-T-X}; Cohesive energy per atom, E_c; in-plane (ν_{in}) and out-of-plane (ν_{out}) Poisson's ratios; 2D Young's modulus, Y_{2D}; Bending stiffness, S_b; and Effective thickness, t_{eff}. Results for structural parameters of TiX_2 (X = S, Se, Te), MoX_2, and WX_2 are in good agreement with the LDA+U results from Ref. [8]. The structure parameters of distorted T compounds, WTe_2 and $MoTe_2$, can be estimated from Supplemental Material Table S2 [62]. The representations of T^{4+} such as d^0, d^2, and d^6 are taken from Ref. [1].

T^{4+}	TMDs	a (Å)	d_{T-X} (Å)	d_{X-X} (Å)	θ_{X-T-X} degree	E_c (eV/atom)	ν_{in}	ν_{out}	Y_{2D} (N/m)	S_b (eV)	t_{eff} (Å)	$Y_{3D}(\frac{Y_{2D}}{t_{eff}})$ (GPa)
d^0	TiS_2	3.42	2.42	2.80	90.16	6.80	0.17	0.42	85.20	2.25	2.25	378.67
	$TiSe_2$	3.55	2.55	3.04	91.76	6.17	0.23	0.43	59.74	2.86	3.03	197.72
	$TiTe_2$	3.76	2.77	3.44	94.55	5.41	0.24	0.38	44.46	3.29	3.77	117.93
	ZrS_2	3.67	2.57	2.87	88.14	7.35	0.19	0.52	83.76	2.13	2.21	379.00
	$ZrSe_2$	3.81	2.70	3.12	90.14	6.71	0.22	0.47	71.30	2.57	2.63	271.10
	$ZrTe_2$	4.01	2.91	3.53	92.94	5.89	0.18	0.44	43.16	3.01	3.66	117.92
	HfS_2	3.62	2.53	2.85	88.65	7.35	0.19	0.52	85.78	2.82	2.51	341.75
	$HfSe_2$	3.75	2.66	3.09	90.37	6.67	0.21	0.47	77.75	3.64	3.00	259.17
	$HfTe_2$	3.98	2.88	3.47	92.58	5.80	0.15	0.41	46.77	3.92	4.01	116.63
d^2	MoS_2	3.17	2.40	3.10	80.56	7.86	0.26	0.30	141.59	12.29	4.08	347.03
	$MoSe_2$	3.30	2.53	3.31	81.86	7.22	0.26	0.32	114.97	14.60	4.94	232.73
	$MoTe_2$-1H	3.51	2.71	3.59	83.04	6.54	0.28	0.34	87.88	14.63	5.65	155.54
	$MoTe_2$-1T'	3.65	–	–	–	6.54	0.28	0.46	61.85	7.28	4.75	130.21
	WS_2	3.16	2.40	3.10	80.25	7.91	0.26	0.33	143.92	12.61	4.10	351.02
	WSe_2	3.29	2.53	3.32	82.16	7.20	0.33	0.35	130.03	14.48	4.62	281.45
	WTe_2-1T'	3.61	–	–	–	6.49	0.35	0.60	86.79	8.96	4.45	195.03
d^6	$PdTe_2$	3.96	2.67	2.73	83.91	4.07	0.32	0.64	61.82	2.78	2.94	210.27
	PtS_2	3.52	2.37	2.45	84.25	5.73	0.29	0.58	105.81	5.66	3.20	330.65
	$PtSe_2$	3.68	2.49	2.60	84.83	5.32	0.26	0.59	87.01	6.33	3.74	232.65
	$PtTe_2$	3.95	2.66	2.74	84.15	5.07	0.26	0.57	81.41	4.58	3.29	247.45

E. Effect of bending on physical properties

1. Local strain

Local strain ($\epsilon = \frac{\delta - \delta_{flat}}{\delta_{flat}}$) profiles projected on the *y-z* plane [see *b-c* plane in Fig. 2(II)] of different TMD nanoribbons corresponding to the bending curvature around 0.09 Å^{-1} are presented in Supplemental Material Fig. S1 [62]. The inner layer gets contracted while the outer layer gets expanded, and this is consistent with the elastic theory of bending of a thin plate [50]. The expansion of the outer layer is close to the contraction of the inner layer for 1T compounds, while the expansion dominates the contraction in the case of 1H compounds (Supplemental Material Fig. S1 [62]). The middle metal layer is expanded up to 2% in the case of 1T while it is 5–10% for 1H, indicating that the middle layer is closer to the neutral axis for 1T than that of the 1H compounds. For 1T′ compounds ($MoTe_2$ and WTe_2), the outer layer is expanded more than the contraction of the inner layer with a distortion represented by the zigzag structure in the strain profile (Supplemental Material Fig. S1 [62]).

To study the effect of bending on the local strain profiles, we compare the local strain profiles of the PtS_2 nanoribbon projected on the *y-z* plane, as shown in Fig. 5. The inner layer is contracted while the outer layer gets expanded. This effect increases upon increasing the bending curvature. For PtS_2, the middle layer is expanded within 2–3%, while the expansion is 16–20% for the inner and the outer layer. Such large local strain can induce a highly nonuniform local potential and hence affect the charge distribution. Both lattice expansion in

the outer layer and the lattice contraction in the inner layer could be applicable in tuning adsorption (binding distance and energy) of the 2D materials, similar to the linear strain modulated adsorption properties of various semiconducting or metallic surfaces [51–53]. The tensile strain strengthens the hydrogen adsorption in TMD surfaces, while a compressive strain weakens it [52]. By utilizing both the concave (compressive strain) and convex (tensile strain) surfaces of a bent monolayer, one can tune the Gibbs free energy of hydrogen adsorption to zero when it is, respectively, more negative and more positive.

2. Physical thickness

The behavior of different layers within the TMD nanoribbon under mechanical bending can be understood by looking at the variation of the physical thickness (t_{tot}, defined later in this section and shown in Fig. 6) with respect to bending curvature. Moreover, tuning of the physical thickness can be particularly useful in nanoelectronic applications due to an enhancement of the electron confinement in 2D materials with an out-of-plane compression [54,55]. A percentage change in the thickness (t_{tot}, t_{up}, or t_{dn}) at the middle of various bent nano-ribbons with respect to the unbent ones is presented in Supplemental Material Fig. S2 [62]. t_{tot} represents an outer-inner chalcogen atom layer thickness at the vertex of a bent ribbon, while t_{up} and t_{dn} correspond to outer-middle and middle-inner layers, respectively. We fitted a sixth-order polynomial to each layer of the bent nanoribbon to estimate the thickness (Supplemental Material Fig. S3 [62]).
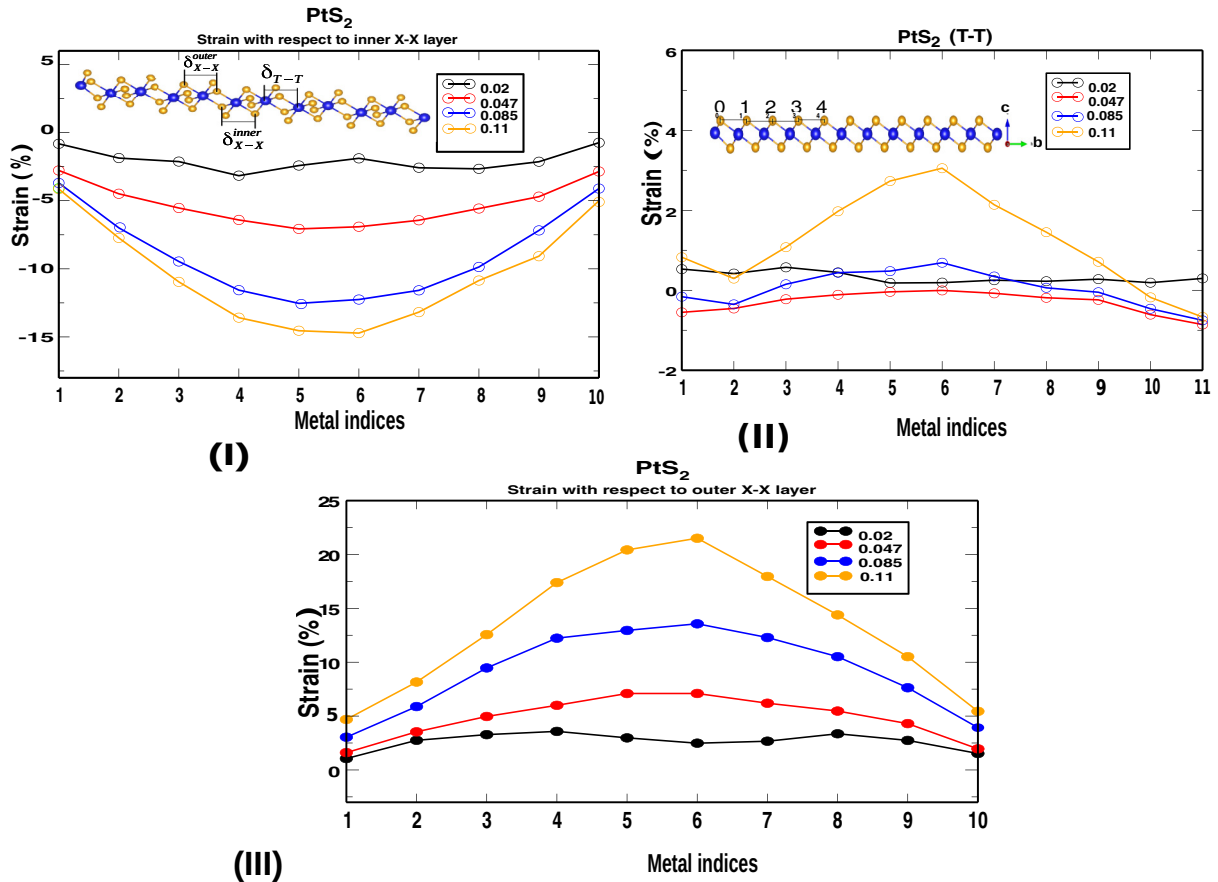
FIG. 5. Local strain ($\epsilon = \frac{\delta - \delta_{\text{flat}}}{\delta_{\text{flat}}}$) with respect to the inner chalcogen-chalcogen ($\epsilon_{\text{X-X}}^{\text{inner}}$), metal-metal ($\epsilon_{\text{T-T}}$), and outer chalcogen-chalcogen distance ($\epsilon_{\text{X-X}}^{\text{outer}}$) projected in the *y-z* plane for PtS$_2$. Strain at metal indices ''*i*'' (see the second subfigure) is calculated with respect to the distance between two metals at indices *i*-1 and *i* where $i = 1, 2, \ldots 10$ (or 11). The legends in figures correspond to different bending curvature (Å^{-1}).

The thickness measured between outer and inner chalcogen layers is described by t_{tot} ($t_{\text{up}} + t_{\text{dn}}$, blue), while t_{up} (red) and t_{dn} (green) are measured between the outer-to-middle and middle-to-inner layers, respectively (see Fig. 6). When a thin plate is bent, it undergoes both compression (z' to N, t_{dn}) and expansion (N to $z' + h$, t_{up}) with "N" being the neutral surface [50] [see Fig. 2(III)]. As the middle layer does not mimic the neutral surface (N), t_{up} and t_{dn} do not, respectively, increase and decrease with the bending curvature. For most of the compounds, t_{up} decreases on increasing the bending curvature. However, t_{dn} slightly increases for d^0-1T compounds, but depends on the bending curvature for d^2-1H and d^6-1T compounds (Supplemental Material Fig. S2 [62]). For a quantitative comparison among different materials, we plot the thicknesses for various TMDs around the bending curvature of 0.09 Å^{-1} as shown in Fig. 6. Group IV compounds have a lower flexural rigidity, therefore have more of a decrement in the physical thickness (t_{tot}) than group VI and X compounds.

F. Effect of the bending on electronic properties

1. Local electronic charge density

Along with the change in physical properties, mechanical bending also affects the electronic properties. The local charge density (average over *a-b* plane [Fig. 2(I)]) is computed and plotted against distance along an out-of-plane direction (*c* axis) [Fig. 2(II)]. The different nature of the local charge distribution of flat WX$_2$ (X=S, Se, Te) ribbon with two equal local maxima may be related to the different pseudopotential used in the calculation. We choose a narrow window (within two black vertical lines) at the middle of a nanoribbon (for both flat and bent) to study the local charge distribution near the surface-vacuum interface as shown in Supplemental Material Fig. S4 [62]. We define three different quantities, width, max, and an area, of the local charge density (left) and compared among the flat nanoribbons of various TMDs (right), as shown in Fig. 7. The "width" represents the distance over which the charge density decays to a smaller nonzero value ($\epsilon < 10^{-4}$) in vacuum (Supplemental Material Fig. S4 [62]) which also gives a tentative idea about the total effective decay length of electron density. In addition, the areal density ($\int_0^{\text{width}} \rho(z) dz$, an area under the curve) represents the average number of electrons per unit area, as shown in Fig. 7.

For the flat nanoribbons, the width increases, whereas max and area decrease as we go from S to Se to Te for a given transition metal. Increasing the width from S to Se to Te indicates an increase in the total effective decay length of electron density, hence the effective thickness. Also, the width corresponding to flat 1H nanoribbons is shifted upward
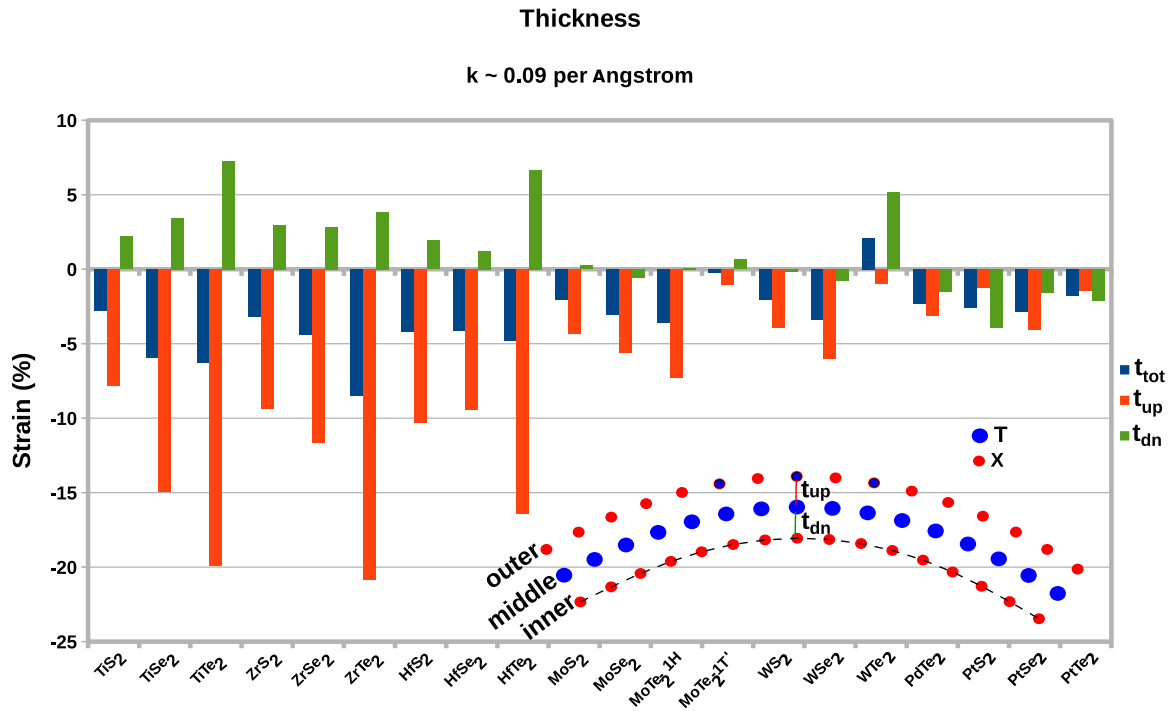
FIG. 6. The strain with respect to the physical thickness of the bent nanoribbon around 0.09 $\mathring{A}^{-1}$ for various TMD compounds; t_{tot} ($t_{up} + t_{dn}$, blue) is outer-inner layer thickness; t_{up} (red) and t_{dn} (green) are measured between outer-middle and middle-inner layers, respectively [see Fig. 2(III)].

by at least 0.5 Å compared to that of 1T flat nanoribbons which then contributes to an effective thickness giving larger bending stiffness. Our results suggest that the overall bending stiffness follows the trend of the width of an electron density and hence the effective thickness. The variation of the local charge density along an out of plane direction for different TMD nanoribbons with the bending curvature is presented in Supplemental Material Fig. S5 [62]. When a nanoribbon is bent, the local charge density shrinks with the bending curvature within an outer layer-vacuum interface while expanding near the inner layer-vacuum interface leaving the total width unaffected. However, both the max and the area decrease with increasing bending curvature for most of the TMD compounds except for TiTe$_2$ and WX$_2$. For WX$_2$, the max. value of local maximum closer to the surface-vacuum interface decreases on increasing the bending curvature (circular region in Supplemental Material Fig. S5 [62]), whereas the other local maxima have an opposite trend. To study the effect of bending on the aforementioned local maximum (max) and areal density (area) among different materials, we estimate their percentage change with respect to the flat ribbon, as in Fig. 7. The bending produces noticeable changes in the charge distribution within the surface-vacuum interfaces.

2. Band structure

The band structure plots of groups IV, VI, and X TMDs with respect to vacuum with various bending curvatures are shown in Supplemental Material Figs. S6, S7, and S8, respectively [62]. The dashed lines in the band structure plots indicate the SCAN estimated Fermi energy with respect to vacuum ("-ve" of the work function) while the red bands

correspond to in-gap edge states. The edge states are identified by comparing the band structures of the ribbon with that of the monolayer bulk, and are highlighted by red color. The bulk band-gap [E_g (eV)] (excluding edge states) and the work function [ϕ (eV)] of our flat nanoribbons are extracted and tabulated in Supplemental Material Table S1 [62]. Out of TMD nanoribbons considered, ZrX$_2$, HfX$_2$, MoY$_2$, and WX$_2$ (X=S, Se; Y=S, Se, Te) are semiconductors. To study the changes in the band structure of these semiconductors with respect to bending, we utilized the hydrogen passivated edges. A few of the low band-gap semiconductors such as TiY$_2$, TTe$_2$ (T=Zr, Hf) and group (X) indirect band-gap semiconductors (PtX$_2$) become metallic due to the edge states. We did not observe any substantial effect of bending on metallic compounds. An effect of the mechanical bending on the band-gap is of particular interest for semiconductors, due to a wide range of applications in nanoelectronics. One each from the 1T and the 1H group, respectively, ZrS$_2$ and MoS$_2$, are chosen to study the effect of bending on the band structure as shown in Fig. 8.

The nature of edge states is different for 1T and 1H semiconductors. The 1T nanoribbon has edge states only below the Fermi level while both the edge states above and below the Fermi level are present in the 1H nanoribbon. The horizontal black dashed lines represent water redox potentials with respect to the vacuum level, −4.44 eV for the reduction (H$^+$/H$_2$), and −5.67 eV for the oxidation (O2/H$_2$O) at pH 0 [56]. When the band edges straddle these potentials, materials possess good water splitting properties. The band edges CB2, VB1 (VBM), and VB2 of MoS$_2$ straddle the water redox potentials while only the edge state CB1 stays within the gap. As semilocal DFT functionals underestimate the band
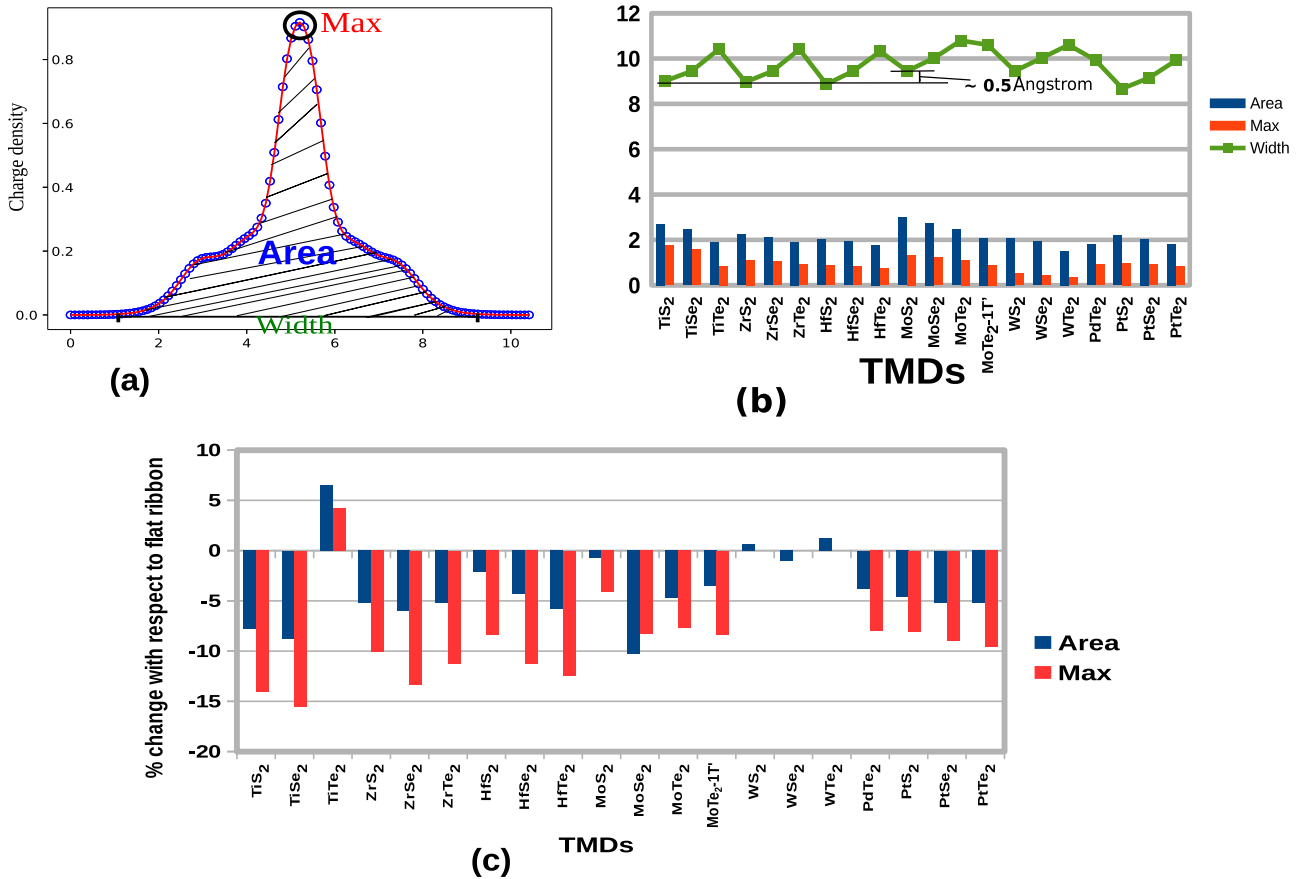
FIG. 7. (a) The local charge density along the out of plane (z) direction of the nanoribbon. (b) Width (Å), max ($e/Å^3$, e: an electronic charge), and areal density ($e/Å^2$) of flat nanoribbon. (c) Percentage change in an area and the max of the bent nanoribbons having a bending curvature around 0.09 Å^{-1} with respect to the flat nanoribbon; result of max. value is not shown for WX_2 as it possesses multiple local maxima.

gap [57], a correction is always expected at the G_0W_0 level (Supplemental Material Table S1 [62]), which shifts the bands above and below the Fermi level even further up and below,

respectively [28]. However, it is known that such correction for localized states (in the case of point defects) is less considerable than that for the delocalized bulk states [58].
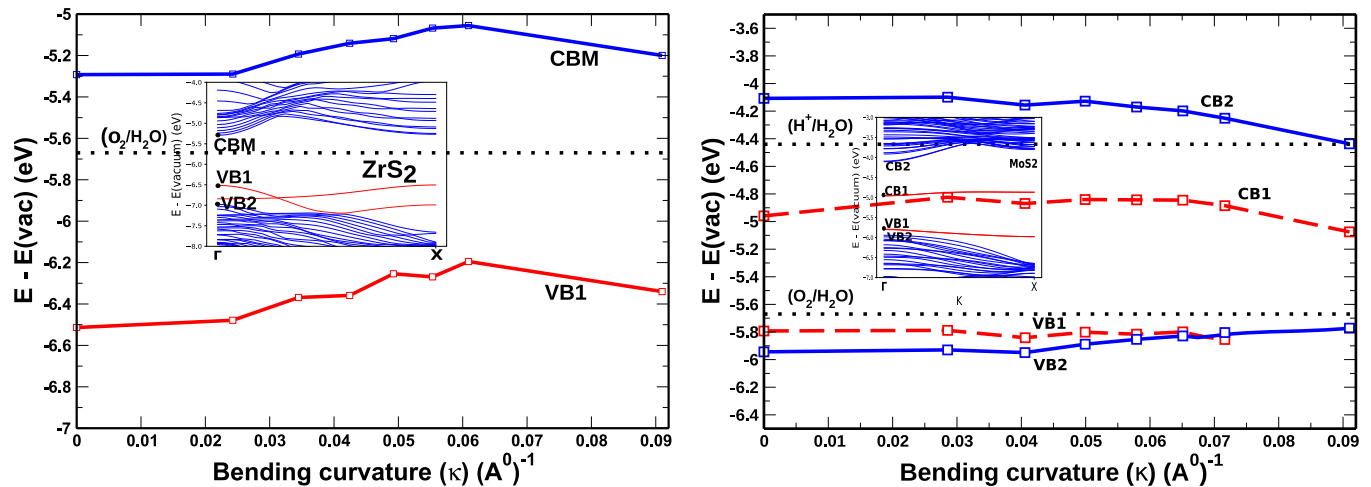
FIG. 8. Variation of band edges with respect to the bending curvature for ZrS_2 (left) and MoS_2 (right); CBM and VB1 are the conduction band minimum and edge state VB (valence band), respectively; CB1 (CBM), CB2, VB1 (VBM), and VB2, respectively, are edge state CB (conduction band), bulk CB, edge state VB (valence band), and bulk VB. For flat MoS_2 ribbon, VB1 represents the VBM while for higher bending curvature ($\kappa = 0.09$ Å^{-1}) VB2 switches to VBM.
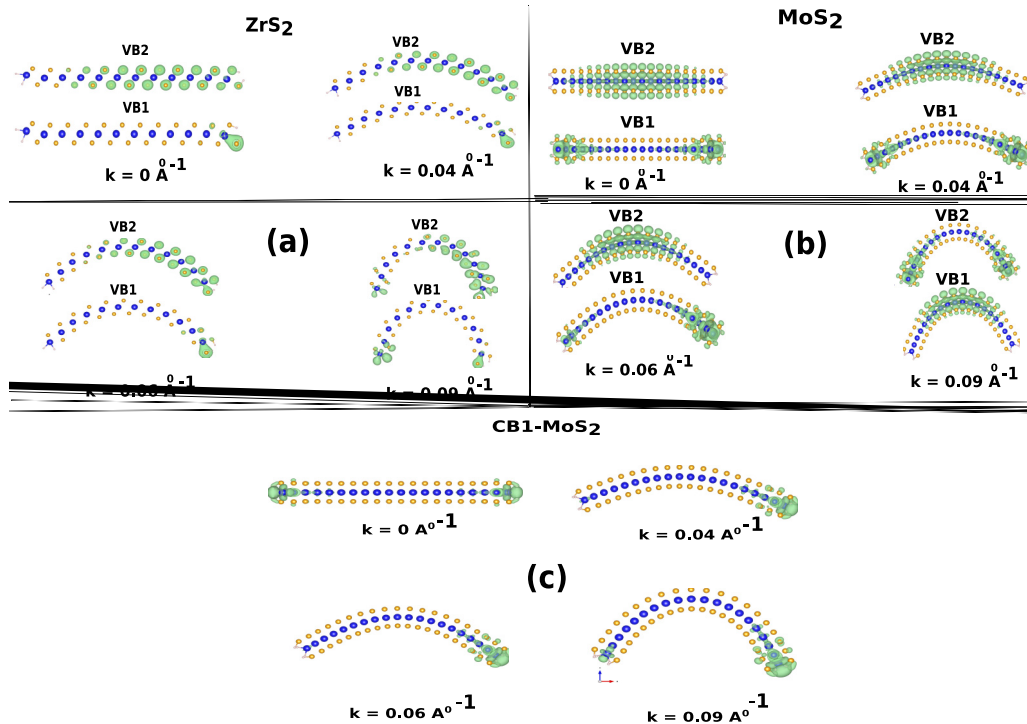
FIG. 9. Variation in the isosurface of partial charge densities at VB1 and VB2 (holes) with respect to the bending curvature; (a) ZrS$_2$; (b) MoS$_2$; (c) Variation in the isosurface of the partial charge densities (donor-like) of MoS$_2$ at CB1 with bending curvatures.

(a) Tuning of band edges. The band edges [conduction band minimum (CBM) and valence band maximum (VBM)] of ZrS$_2$ and other 1T semiconductors increase on increasing the bending curvature, while this varies from one band edge to another for MoS$_2$ and other 1H semiconductors. For example, shifting of the band energies with respect to vacuum is negligible for edge states as compared to the bulk ones for MoS$_2$. The shifting of band edges also leads to changing of the Fermi level as well as the band gap (Supplemental Material Fig. S10 [62]). For MoS$_2$, VB2 increases while VB1 decreases on increasing the bending curvature and eventually results in the removal of some of the edge states, though, complete elimination might not be possible. Since the mechanical bending shifts the band edges only by a little, the photocatalytic properties of MoS$_2$ and WS$_2$ is preserved even for a larger bending curvature. On the other hand, bending can shift the band edges of 1T semiconductors by a considerable amount for bending curvature up to 0.06 Å^{-1}, but shift downward for higher bending curvature. For example, one can shift the band edges of ZrS$_2$ upward by 0.25 eV when applying the bending curvature of 0.06 Å^{-1}. Moreover, the G$_0$W$_0$ calculated band structure shows that the CBM (−4.58 and −4.53 eV, respectively) of ZrS$_2$ and HfS$_2$ is slightly lower than the reduction potential (−4.44 eV) while the VBM (−7.15 and −6.98 eV) is significantly lower than the water oxidation potential (−5.67 eV) [59]. Mechanical bending can shift the band edges in the upward direction to straddle the water redox potentials, enhancing the photocatalytic activity. The effect of bending on the band edges of 1H-TSe$_2$ semiconductors is different than that of 1H-TS$_2$ (Supplemental Material Fig. S9 [62]), especially in the bulk valence band maximum (VB2).

The VB2 is almost constant for lower bending curvature for TSe$_2$, while there is an appreciable increase in the case of TS$_2$.

(b) Charge localization and conductivity. In this section, we describe the effect of bending on band edges in terms of localization or delocalization of the charge carriers at those band edges. The variation of an isosurface of the partial charge (electrons or holes) density with respect to bending curvature are presented in Figs. 9 and 10. Using the mechanical bending, one can tune the conductivity of TMD monolayers [28]. Before bending, the charge carriers (holes) of ZrS$_2$ at VB2 are delocalized over the whole ribbon width, decreasing in
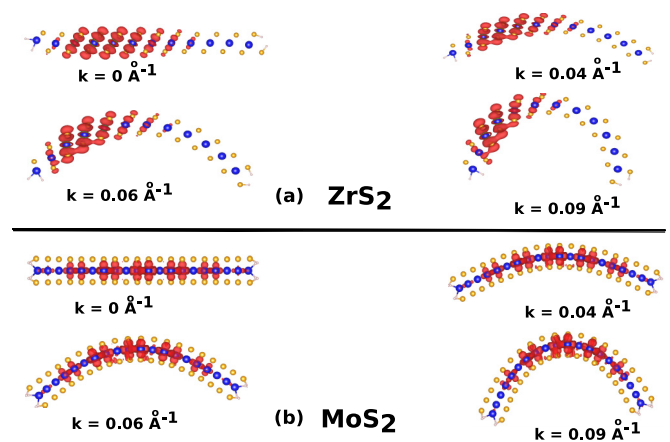

FIG. 10. Variation in the isosurface of partial charge density (electrons) with respect to the bending curvature at bulk conduction band minimum; (a) CBM for ZrS$_2$; (b) CB2 for MoS$_2$.
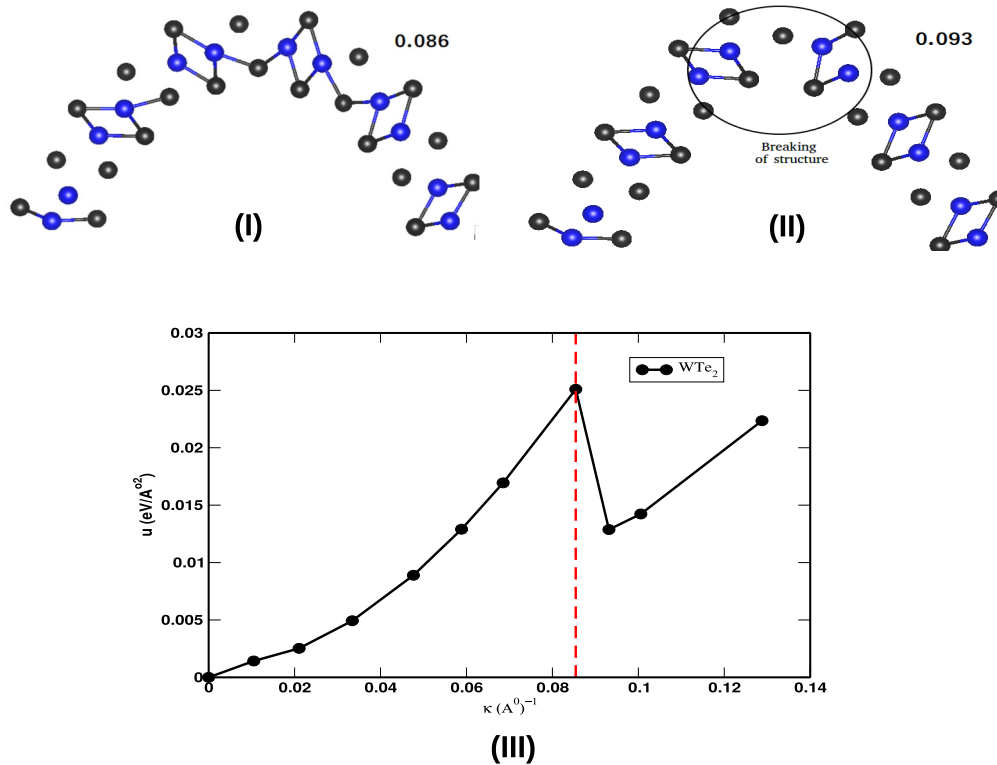
FIG. 11. (I, II): Structures for 2 different bending curvatures, showing the breaking of the ribbon within the curvature region; The figure on left is for $\kappa = 0.086$ Å^{-1} while the one on the right is for $\kappa = 0.093$ Å^{-1}. (III) An areal bending energy density with respect to bending curvature for WTe$_2$, showing the breaking of structure.

magnitude from S-edge to Zr-edge. The mechanical bending localizes the charges towards the S-edge while depleting along the Zr-edge, reducing the conductivity from one edge to the other. However, the charge density on top of VB1 does not change much with the bending for lower bending curvatures. However, at $\kappa = 0.09$ Å^{-1} some charges accumulate at the Zr-edge, thereby changing the trend of band energy with respect to vacuum (see Fig. 8). Unlike ZrS$_2$, the charge carriers (holes) of MoS$_2$ at VB2 are delocalized over the whole width, decrease in magnitude from the center of the ribbon to either side of edges symmetrically. With bending, the charge carriers localize at the middle of the ribbon and deplete at the edges, reducing the conductivity due to holes from one edge to the other [28]. At a higher bending curvature beyond $\kappa > 0.065$ Å^{-1}, edge state VB1 crosses the bulk-VB and becomes VB2 and vice versa. Similar to VB1, CB1 also has the same behavior before and after bending, except it does not cross the CB2. Instead, it is also shifted down as VB1 does.

Conversely, the charge carriers (electrons) of ZrS$_2$ at the CBM (CB2) decrease in magnitude from Zr-edge to the S-edge. Again, mechanical bending localizes the electrons towards the Zr-edge. However, the electronic conductivity does not change even for larger bending curvature for MoS$_2$. The electrons are delocalized uniformly over the whole ribbon width which remains unaffected for a wide range of bending curvature. The conductivity of a semiconductor is the sum of conductivity of both electrons and holes. The mechanical bending reduces both types of conductivity in 1T

nductors, while it only reduces hole-type conductivity in 1H semiconductors.

G. Stability of nanoribbons and finite width effect

Based on our calculation, we have found that the stability of the flat nanoribbons also depends on the type of edge. We have taken stoichiometric (n(X):n(T) = 2:1) nanoribbons (Supplemental Material Fig. S4 [62]) for most of the calculations. However, we could not relax TiSe$_2$, HfS$_2$, PdTe$_2$, and PtSe$_2$ nanoribbons in this configuration. We confirm that the instability of these flat ribbons cannot be removed simply by increasing the width of the ribbon. We chose a symmetric edge nanoribbon by removing 2 dangling X (S, Se, or Te) atoms from one of the edges for these compounds (Fig. 2 II). Our calculation shows that the TMD nanoribbons are stable against mechanical bending for a wide range of bending curvature, except for WTe$_2$. The bond breaking at the curvature region is observed for $\kappa > 0.086$ Å^{-1}, as shown in Fig. 11. Upon bending, one of the chalcogen atoms in the curvature region moves towards the middle layer, causing a further separation of the two metal atoms, as shown inside the circle, creating a sudden jump, as shown in an areal bending energy density versus curvature plot [see Fig. 11(III)].

We utilized the thin plate bending model in our assessment in which we fix the width between flat and bent nanoribbons. It eliminates the quantum confinement effect present in the nanotube method due to dissimilarity of the width between flat and bent nanoribbons of the different radii of curvatures.

However, the edge effects due to the finite width may remain uneliminated. González *et al.* [60], using classical molecular dynamics simulation, reported that the bending stiffness of MoS_2 estimated with a 0.95 nm width nanoribbon is only 46% of those estimated using an 8-nm-wide nanoribbon. But, it recovers 88–93% of bending stiffness when the width increases up to 3–4 nm, leaving the overall trend unaffected. We believe that such an accuracy would be a reasonable tradeoff to the computational complexity that arises while using a larger width. Moreover, we expect that the finite size effect would be less present in our results than in those calculated from MD simulation, as the quantum effects are more properly treated.

IV. CONCLUSION AND DISCUSSION

The 2D materials offer a wide range of electronic properties efficiently applicable in sensors, energy storage, photonics, and optoelectronic devices. The higher flexural rigidity and strain-tunable properties of these compounds make them potential functional materials for future flexible electronics. In this work, we have employed the SCAN functional to explore the physical and mechanical properties of the 2D transition metal dichalcogenide (TMD) monolayers under mechanical bending. SCAN performs reasonably well in predicting the correct ground-state phase as well as the geometrical properties. Also, a wide variety of flexural rigidities can be observed while scanning the periodic table for TMDs. The in-plane stiffness decreases from S to Se to Te, while the bending stiffness has the opposite trend. Overall, the bending stiffness also depends on the d band filling in the transition metal. The bending stiffness increases on increasing the filling of the d band from sparsely filled (d^0) to nearly half-filled (d^2). However, decrease in bending stiffness is observed on moving from nearly half-filled (d^2) to completely filled (d^6) d band. The out-of-plane Poisson's ratios are found to be different from the in-plane Poisson's ratio for 1T and 1T′ monolayers, while the difference is negligible in the case of 1H compounds, showing an anisotropic behavior of 1T and 1T′ monolayers.

Despite the extraordinary physical and electronic properties of TMDs, there are still challenges to make use of TMD semiconductors in nanoelectronics. The strong Fermi level pinning and high contact resistance are key bottlenecks in contact-engineering which are mainly due to in-plane, in-gap edge states and do not depend too much on the work function of a contact metal [61]. Thanks to mechanical bending, tuning of various properties of monolayer TMDs is possible, including band edges, thickness, and local strain. Bending deformation produces highly nonuniform local strain up to 40% (Supplemental Material Fig. S1 [62]), which is almost impossible with a linear strain (ϵ). The high out-of-plane compressive strain developed within the layers due to bending reduces the mechanical thickness and makes the materials thinner in the curvature region. Moreover, one can remove strong Fermi-level pinning while using it in contact-engineering. Besides that, the optimal band alignment with the HER redox potential can be achieved for 1T semiconductors ZrS_2 and HfS_2 under mechanical bending, which are not present in an unbent monolayer. Furthermore, both electron and hole conductivities are affected in 1T semiconductors, while only the hole conductivity is affected in 1H semiconductors [28]. Similar to graphene [46–49], the estimated effective thickness of group IV TMDs, especially sulfide and selenide, is underestimated as compared to chalcogen-chalcogen distance (d_{X-X}), which is quite puzzling and needs further investigation.

[1] J. Wilson and A. Yoffe, Adv. Phys. **18**, 193 (1969).

[2] M. Xu, T. Liang, M. Shi, and H. Chen, Chem. Rev. **113**, 3766 (2013).

[3] A. V. Kolobov and J. Tominaga, *Two-Dimensional Transition-Metal Dichalcogenides*, Vol. 239 (Springer, Berlin, 2016).

[4] C. Tsai, F. Abild-Pedersen, and J. K. Nørskov, Nano Lett. **14**, 1381 (2014).

[5] P. Johari and V. B. Shenoy, ACS Nano **6**, 5449 (2012).

[6] M. Chhowalla, H. S. Shin, G. Eda, L.-J. Li, K. P. Loh, and H. Zhang, Nat. Chem. **5**, 263 (2013).

[7] L. Yu, Q. Yan, and A. Ruzsinszky, Nat. Commun. **8**, 15224 (2017).

[8] C. Ataca, H. Sahin, and S. Ciraci, J. Phys. Chem. C **116**, 8983 (2012).

[9] D. Akinwande, N. Petrone, and J. Hone, Nat. Commun. **5**, 5678 (2014).

[10] Q. H. Wang, K. Kalantar-Zadeh, A. Kis, J. N. Coleman, and M. S. Strano, Nat. Nanotechnol. **7**, 699 (2012).

[11] K. He, C. Poole, K. F. Mak, and J. Shan, Nano Lett. **13**, 2931 (2013).

[12] G. Casillas, U. Santiago, H. Barrón, D. Alducin, A. Ponce, and M. José-Yacamán, J. Phys. Chem. C **119**, 710 (2014).

[13] K. Lai, W.-B. Zhang, F. Zhou, F. Zeng, and B.-Y. Tang, J. Phys. D: Appl. Phys. **49**, 185301 (2016).

[14] D.-U. Jin, J.-S. Lee, T.-W. Kim, S.-G. An, D. Straykhilev, Y.-S. Pyo, H.-S. Kim, D.-B. Lee, Y.-G. Mo, H.-D. Kim *et al.*, in *SID Symposium Digest of Technical Papers*, Vol. 40 (Wiley Online Library, New York, 2009), pp. 983–985.

[15] L. Zhou, A. Wanga, S.-C. Wu, J. Sun, S. Park, and T. N. Jackson, Appl. Phys. Lett. **88**, 083502 (2006).

[16] F. R. Rothkopf, Cover attachment with flexible display, U.S. Patent No. 9,335,793 (2016).

[17] W. S. Wong and A. Salleo, *Flexible Electronics: Materials and Applications*, Vol. 11 (Springer Science & Business Media, Berlin, 2009).

[18] M. Stoppa and A. Chiolerio, Sensors **14**, 11957 (2014).

[19] D.-H. Kim, R. Ghaffari, N. Lu, and J. A. Rogers, Annu. Rev. Biomed. Eng. **14**, 113 (2012).

[20] J. R. Windmiller and J. Wang, Electroanalysis **25**, 29 (2013).

[21] G. Schwartz, B. C.-K. Tee, J. Mei, A. L. Appleton, D. H. Kim, H. Wang, and Z. Bao, Nat. Commun. **4**, 1859 (2013).

[22] S. Park, H. Kim, M. Vosgueritchian, S. Cheon, H. Kim, J. H. Koo, T. R. Kim, S. Lee, G. Schwartz, H. Chang *et al.*, Adv. Mater. **26**, 7324 (2014).

[23] M. L. Hammock, A. Chortos, B. C.-K. Tee, J. B.-H. Tok, and Z. Bao, Adv. Mater. **25**, 5997 (2013).

[24] D. Akinwande, C. J. Brennan, J. S. Bunch, P. Egberts, J. R. Felts, H. Gao, R. Huang, J.-S. Kim, T. Li, Y. Li *et al.*, Extreme Mech. Lett. **13**, 42 (2017).

[25] J.-W. Jiang, Z. Qi, H. S. Park, and T. Rabczuk, Nanotechnology **24**, 435705 (2013).

[26] S. Xiong and G. Cao, Nanotechnology **27**, 105701 (2016).

[27] J. Zhao, Q. Deng, T. H. Ly, G. H. Han, G. Sandeep, and M. H. Rümmeli, Nat. Commun. **6**, 8935 (2015).

[28] L. Yu, A. Ruzsinszky, and J. P. Perdew, Nano Lett. **16**, 2444 (2016).

[29] D. H. Robertson, D. W. Brenner, and J. W. Mintmire, Phys. Rev. B **45**, 12592 (1992).

[30] M. Arroyo and T. Belytschko, Phys. Rev. B **69**, 115415 (2004).

[31] Y. Huang, J. Wu, and K.-C. Hwang, Phys. Rev. B **74**, 245413 (2006).

[32] J. Hafner, J. Comput. Chem. **29**, 2044 (2008).

[33] P. E. Blöchl, Phys. Rev. B **50**, 17953 (1994).

[34] G. Kresse and D. Joubert, Phys. Rev. B **59**, 1758 (1999).

[35] G. Kresse, http://cms.mpi.univie.ac.at/vasp/ (2001).

[36] J. Sun, A. Ruzsinszky, and J. P. Perdew, Phys. Rev. Lett. **115**, 036402 (2015).

[37] N. K. Nepal, A. Ruzsinszky, and J. E. Bates, Phys. Rev. B **97**, 115140 (2018).

[38] J. Sun, R. C. Remsing, Y. Zhang, Z. Sun, A. Ruzsinszky, H. Peng, Z. Yang, A. Paul, U. Waghmare, X. Wu, M. L. Klein, and J. P. Perdew, Nat. Chem. **8**, 831 (2016).

[39] C. Shahi, J. Sun, and J. P. Perdew, Phys. Rev. B **97**, 094111 (2018).

[40] I.-G. Buda, C. Lane, B. Barbiellini, A. Ruzsinszky, J. Sun, and A. Bansil, Sci. Rep. **7**, 44766 (2017).

[41] H. J. Monkhorst and J. D. Pack, Phys. Rev. B **13**, 5188 (1976).

[42] W. Choi, N. Choudhary, G. H. Han, J. Park, D. Akinwande, and Y. H. Lee, Mater. Today **20**, 116 (2017).

[43] S. Aminalragia-Giamini, J. Marquez-Velasco, P. Tsipas, D. Tsoutsou, G. Renaud, and A. Dimoulas, 2D Mater. **4**, 015001 (2016).

[44] G. Lucovsky, R. M. White, J. A. Benda, and J. F. Revelli, Phys. Rev. B **7**, 3859 (1973).

[45] S. Bertolazzi, J. Brivio, and A. Kis, ACS Nano **5**, 9703 (2011).

[46] B. I. Yakobson and R. E. Smalley, Am. Sci. **85**, 324 (1997).

[47] Q. Wang, Int. J. Solids Struct. **41**, 5451 (2004).

[48] K. N. Kudin, G. E. Scuseria, and B. I. Yakobson, Phys. Rev. B **64**, 235406 (2001).

[49] X. Zhou, Phys. Rev. B **62**, 13692 (2000).

[50] L. D. Landau and E. M. Lifshitz, *Theory of Elasticity*, Vol. 7, 2nd ed. (Pergamon Press, London, 1986).

[51] L. Kou, A. Du, C. Chen, and T. Frauenheim, Nanoscale **6**, 5156 (2014).

[52] X. Chen and G. Wang, Phys. Chem. Chem. Phys. **18**, 9388 (2016).

[53] M. Mavrikakis, B. Hammer, and J. K. Nørskov, Phys. Rev. Lett. **81**, 2819 (1998).

[54] M. Brooks and G. Burkard, Phys. Rev. B **97**, 195454 (2018).

[55] Á. M. García, E. del Corro, M. Kalbac, and O. Frank, Phys. Chem. Chem. Phys. **19**, 13333 (2017).

[56] V. Chakrapani, J. C. Angus, A. B. Anderson, S. D. Wolter, B. R. Stoner, and G. U. Sumanasekera, Science **318**, 1424 (2007).

[57] J. P. Perdew, Int. J. Quant. Chem. **28**, 497 (1985).

[58] A. Alkauskas, P. Broqvist, and A. Pasquarello, Phys. Rev. Lett. **101**, 046405 (2008).

[59] H. L. Zhuang and R. G. Hennig, J. Phys. Chem. C **117**, 20440 (2013).

[60] R. I. González, F. J. Valencia, J. Rogan, J. A. Valdivia, J. Sofo, M. Kiwi, and F. Munoz, RSC Adv. **8**, 4577 (2018).

[61] C. Kim, I. Moon, D. Lee, M. S. Choi, F. Ahmed, S. Nam, Y. Cho, H.-J. Shin, S. Park, and W. J. Yoo, ACS Nano **11**, 1588 (2017).

[62] See Supplemental Material at http://link.aps.org/supplemental/10.1103/PhysRevMaterials.3.073601 for supplementary tables and figures describing structures, computational setups, and various electronic as well as mechanical properties referenced in the manuscript.